A coupled volume-of-fluid/immersed-boundary method for the study of propagating waves over complex-shaped bottom: Application to the solitary wave

Simon Gsell, Thomas Bonometti, Dominique Astruc

▶ **To cite this version:**

Simon Gsell, Thomas Bonometti, Dominique Astruc. A coupled volume-of-fluid/immersed-boundary method for the study of propagating waves over complex-shaped bottom: Application to the solitary wave. Computers and Fluids, 2016, 131, pp.56-65. 10.1016/j.compfluid.2016.03.013 . hal-01293270

HAL Id: hal-01293270
https://hal.science/hal-01293270

Submitted on 24 Mar 2016

HAL is a multi-disciplinary open access archive for the deposit and dissemination of scientific research documents, whether they are published or not. The documents may come from teaching and research institutions in France or abroad, or from public or private research centers.

L'archive ouverte pluridisciplinaire **HAL**, est destinée au dépôt et à la diffusion de documents scientifiques de niveau recherche, publiés ou non, émanant des établissements d'enseignement et de recherche français ou étrangers, des laboratoires publics ou privés.

Open Archive TOULOUSE Archive Ouverte (OATAO)
OATAO is an open access repository that collects the work of Toulouse researchers and makes it freely available over the web where possible.

This is an author-deposited version published in : http://oatao.univ-toulouse.fr/
Eprints ID : 15650

To link to this article : DOI:10.1016/j.compfluid.2016.03.013
URL : http://dx.doi.org/10.1016/j.compfluid.2016.03.013

To cite this version :
Gsell, Simon and Bonometti, Thomas and Astruc, Dominique *A coupled volume-of-fluid/immersed-boundary method for the study of propagating waves over complex-shaped bottom: Application to the solitary wave.* (2016) Computers and Fluids, vol. 131. pp. 56-65. ISSN 0045-7930

Any correspondence concerning this service should be sent to the repository administrator: staff-oatao@listes-diff.inp-toulouse.fr

A coupled volume-of-fluid/immersed-boundary method for the study of propagating waves over complex-shaped bottom: Application to the solitary wave

Simon Gsell*, Thomas Bonometti, Dominique Astruc

Institut de Mécanique des Fluides de Toulouse, UMR No 5502 CNRS-INPT-UPS, Allée du Prof. Camille Soula, F-31400 Toulouse, France

A B S T R A C T

We report about a numerical approach based on the direct numerical simulation of the Navier–Stokes equations for the study of wave-bottom interaction problems. A Volume of Fluid (VOF) method is coupled with an Immersed Boundary Method (IBM) and applied to the simulation of propagating waves over complex shaped bottoms. We first investigate the flow induced by a solitary wave over generic bottoms (i.e. a semi-circular cylinder and a sloping beach). We show that the method is able to describe various important features of wave-bottom interactions, including flow separation, vortex shedding and wave breaking, while keeping a reasonable computational effort. Then we demonstrate the capability of the present approach to model arbitrary shaped bottoms by simulating the run-up of a breaking solitary wave over a natural beach profile.

Keywords:
VOF
IBM
Solitary wave
Wave-bottom interactions
Wave shoaling
Wave breaking

1. Introduction

After being generated in the open sea by wind or geophysical events, gravity waves propagate toward the coast, carrying a considerable amount of energy. Close to the shore, the wave dynamics changes as a result of the interaction with the bottom. This is the shoaling process, which may include wave breaking. Knowing the mechanisms that take place during the wave shoaling is a key issue for many engineering applications involving sediment transport, civil engineering, shore protection and energy extraction. During the last decades, numerical simulation has proved to be a promising tool for the study of wave-body and wave-bottom interaction problems, as demonstrated by the wide variety of numerical methods applied to the study of waves interacting with a submerged body in the literature (e.g. [1–3]).

Many studies of surface waves are based on potential flow theory, under the assumption of irrotational and inviscid flow. The fluid equations are usually reduced to a Laplace equation for the velocity potential and a set of non-linear boundary conditions. Two families of numerical techniques using potential flow theory are the Boundary Element Methods [4–7] and the Spectral Methods [1,8–11] which are based on pertubative expansions and are able to model both constant- and variable-depth problems [12,13]. When viscous effects such as vortex shedding and energy dissipation in the boundary layers have to be locally taken into account to describe the wave dynamics, potential flow models can be coupled with a Navier–Stokes solver through a domain decomposition approach [14–16]. Note that Lin and Huang [2,17] also proposed a vortex method to take into account the generation and shedding of vorticity due to the presence of a solid body.

Another class of numerical techniques is based on the long wave theory using in particular the Boussinesq equations (e.g. [18,19]) and the non-linear shallow-water equations [20–22]. The similarity between shallow-water and gas dynamics equations allows to apply efficient shock-capturing schemes, initially developed for Euler equations, to investigate bore dynamics resulting from breaking waves [23,24]. However, as both the non-linear shallow-water and the Boussinesq equations are based on hydrostatic or almost hydrostatic approximation, they fail to predict the complex interaction between a wave and a bottom of arbitrary shape.

In order to capture all the flow characteristics resulting from a wave-body interaction problem, one may rather choose to solve the full incompressible Navier–Stokes equations. A major challenge raised by this numerical strategy deals with the treatment of the free surface dynamics.

Various techniques using boundary-fitted moving grids have been used [3,25–27]. These methods allow an accurate interface tracking as the mesh fits the shape of the free surface. However, it can hardly be applied to complex interface deformations as wave breaking. Eulerian methods allow instead to use a fixed

* Corresponding author. Tel.: +33534322912.
E-mail address: simon.gsell@imft.fr (S. Gsell).

http://dx.doi.org/10.1016/j.compfluid.2016.03.013

grid on which the interface is free to deform. The capture of the interface is ensured by the convective transport of either a finite number of markers or a continuous function. In particular, the Volume of Fluid (VOF) method has been extensively used for the study of wave-breaking and wave run-up [28–31] as well as wave-body interaction [32–34]. This method has been shown to be able to deal with complex phenomenon as wave breaking and air entrainment. When the shape of the bottom remains simple, it is convenient to use a boundary-fitted grid associated with a no-slip condition. However, with such a method the computational effort rapidly increases when increasing the geometrical complexity of the boundaries. In order to treat wave dynamics problems with increasing complexity while keeping a reasonable computational cost, VOF-type methods can be coupled with Immersed Boundary Methods (IBM). The IBM technique enables to place bodies of arbitrary shape in a computational domain discretized with a structured Cartesian grid. This numerical approach has already been applied to the interaction between surface waves and submerged obstacles [35–37]. In this type of configuration, the water/air interface does not cross the water/body interface. More recently, physical configurations involving partially immersed bodies (water entry of a sphere and dam break with an obstacle) have been investigated by Zhang et al. [38] and Zhao et al. [39].

In this paper, a coupled VOF-IBM method is used to simulate the flow induced by a solitary wave interacting with a complex shaped bottom. The numerical method is applied to geometries of increasing complexity. Both submerged and partially immersed obstacles are considered. We first investigate the flow induced by a solitary wave interacting with a submerged semi-circular cylinder, showing that our results are in good agreement with those of Kletter and Eames [3] which were obtained with a boundary-fitted approach. Then, the run-up of non-breaking and breaking solitary waves on a sloping beach is investigated and compared to detailed experiments of Synolakis [40]. Finally, we present simulations of the run-up of a breaking solitary wave on a natural beach of complex topography, the shape of which being the result of wave-induced sediment transport observed in laboratory experiments.

2. Numerical method

2.1. Governing equations and assumptions

Let us consider two immiscible fluids, i.e. air and water, of density ρ_a and ρ_w, and dynamic viscosity μ_a and μ_w, respectively. We assume the two fluids to be Newtonian and incompressible. Considering relatively large amplitude gravity waves, we neglect the surface tension effects in the following. The evolution of the two-phase flow is then described by the one-fluid formulation of the Navier–Stokes equations [41], namely

$$\frac{\partial \mathbf{V}}{\partial t} + \nabla \cdot (\mathbf{V} \otimes \mathbf{V}) = \mathbf{g} - \frac{1}{\rho}\nabla P + \frac{1}{\rho}\nabla \cdot [\mu(\nabla \mathbf{V} + \nabla \mathbf{V}^T)] + \mathbf{f}, \quad (1)$$

$$\nabla \cdot \mathbf{V} = 0, \quad (2)$$

where $\mathbf{V}$, P, ρ and μ denote the local velocity, pressure, density and viscosity in the flow, respectively, $\mathbf{g}$ denotes gravity and $\mathbf{f}$ is a volume force term used to take into account solid-fluid interaction. The local volume fraction C of the air obeys

$$\frac{\partial C}{\partial t} + (\mathbf{V} \cdot \nabla)C = 0. \quad (3)$$

This volume fraction equals one (resp. zero) in cells filled with air (resp water) while values of volume fraction lying between 0 and 1 indicate the presence of an air-water interface. The local density and viscosity are computed from the volume fraction as $\rho = C\rho_a + (1-C)\rho_w$ and $\mu = C\mu_a + (1-C)\mu_w$, respectively. In the present method, no interface reconstruction step is employed so the numerical thickness of the interface is not strictly zero, but typically spreads over three grid cells [42]. Eqs. (1)-(3) are solved throughout the entire computational domain, including the actual fluid domain and the space occupied by the solid.

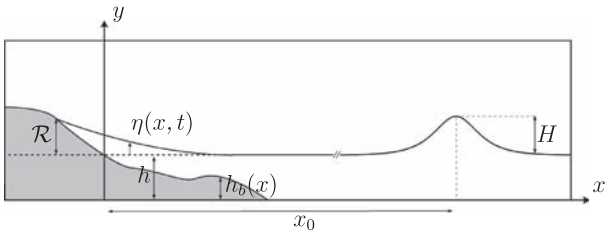

Fig. 1. Schematic view of the set-up. The solitary wave of amplitude H and depth h is initially placed at x_0. The vertical position of the air-water interface is $h+\eta$ while that of the intersection point between the air-water interface and the immersed boundary is $y = h + \mathcal{R}$, $\mathcal{R}$ being the run-up elevation.

2.2. Modeling of the immersed solid

Following the IBM method [41], the interaction between the fluid and the immersed body is carried out by the addition of a volume force term $\mathbf{f}$ in (1). We first define a solid volume fraction $\alpha(\mathbf{x})$ accounting for the presence of the immersed solid. The value of the parameter α is set to 1 in the solid region and 0 in the fluid region. A transition region is introduced, where α values are laying between 0 and 1. Here we consider the particular case of fixed bottom or bottom-seated obstacles. Assuming that the bottom shape is described by a function $h_b(x)$ (see Fig. 1), we define the solid volume fraction as [41]

$$\alpha(\mathbf{x}) = \frac{1}{2}\left\{1 - tanh\left(\frac{y - h_b(x))}{\lambda \eta_i \Delta}\right)\right\} \quad (4)$$

$$\lambda = |n_x| + |n_y| + |n_z| \quad (5)$$

$$\eta_i = 0.065(1 - \lambda^2) + 0.39 \quad (6)$$

where $\mathbf{n} = (n_x, n_y, n_z)$ is the normal outward unit vector at the surface, η_i is a parameter controlling the thickness of the transition region and Δ is a characteristic grid size ($\Delta = \sqrt{2}\Delta x$ for a 2D uniform grid). The force $\mathbf{f}$ is then defined as

$$\mathbf{f} = \alpha \frac{\mathbf{V}_s - \tilde{\mathbf{V}}}{\Delta t}, \quad (7)$$

where Δt is the time step used for the time-advancement, $\mathbf{V}_s$ is the local velocity imposed in the solid object ($\mathbf{V}_s = 0$ here), and $\tilde{\mathbf{V}}$ is an intermediate velocity field without considering the immersed object. For more precision, see Section 2.4.

2.3. Time stepping and spatial discretization

Eqs. (1) –(3) are solved on a staggered Cartesian grid following a finite-volume approach [43]. The time integration of (1) and (2) is performed via a third-order Runge–Kutta method for all terms except the viscous term for which a second-order semi-implicit Crank–Nicolson scheme is used [44]. The incompressibility condition (2) is satisfied at the end of each time step through a projection method. The transport equation of volume fraction (3) is solved by using a modified version of the flux-corrected transport scheme proposed by Zalesak [45]. Domain decomposition and Message-Passing-Interface (MPI) parallelization is performed to facilitate simulation of large number of computational cells.

2.4. Summary of the time-advancement procedure

The time-advancement procedure of the present coupled VOF-IBM method within a time-step is described in the following, in the specific case of a fixed immersed object.

1. At the beginning of the time step, the divergence-free velocity field $\mathbf{V}^n$, volume fraction C^n, pressure $P^{n-1/2}$ in the fluid are known, where n refers to the time step.
2. C^{n+1} is computed by solving (3), and second-order approximations of the volume fraction $C^{n+1/2}$ at time $(n+1/2)\Delta t$ are computed using $C^{n+1/2} = (C^n + C^{n+1})/2$, and used to estimate fluid density and viscosity in Eq. (1).
3. A Mixed Runge–Kutta/Crank–Nicolson loop $(k = 1, 2, 3)$ is used to compute the velocity field predictor $\widehat{\mathbf{V}}^{n+1}$, taking into account the presence of the solid body but not respecting the divergence free condition.

3a. Computation of the intermediate velocity field $\widetilde{\mathbf{V}}^k$ without considering fluid-solid interaction:

$$\frac{\widetilde{\mathbf{V}}^k - \widehat{\mathbf{V}}^{k-1}}{\Delta t} = \mathcal{SM}, \tag{8}$$

with

$$\mathcal{SM} = \gamma_k \mathbf{N}(\widehat{\mathbf{V}}^{k-1}) + \zeta_k \mathbf{N}(\widehat{\mathbf{V}}^{k-2}) + (\alpha_k + \beta_k)\mathbf{L}(\widehat{\mathbf{V}}^{k-1}) - (\alpha_k + \beta_k)\left(\frac{1}{\rho}\nabla P^{n-1/2} - \mathbf{g}\right) \tag{9}$$

where $\mathbf{N}$ (resp. $\mathbf{L}$) is the non-linear (resp. linear) operator for the advective (resp. viscous) terms. α_k, β_k, γ_k and ζ_k are the Runge–Kutta coefficients. The velocity predictor $\widehat{\mathbf{V}}^k$ is initialized with the velocity field at the previous time step.

3b. Computation of the velocity field which includes the contribution of the fluid-solid coupling term $\mathbf{f}^k$ (the calculation of which does not make use of an internal loop) as

$$\mathbf{f}^k = \alpha \frac{-\widetilde{\mathbf{V}}^k}{\Delta t}, \tag{10}$$

$$\frac{\widehat{\mathbf{V}}^k - \widehat{\mathbf{V}}^{k-1}}{\Delta t} - \beta_k \mathbf{L}(\widehat{\mathbf{V}}^k - \widehat{\mathbf{V}}^{k-1}) = \mathcal{SM} + \mathbf{f}^k. \tag{11}$$

3c. For $k = 3$, $\widehat{\mathbf{V}}^{n+1}$ is then obtained.

4. In order to verify Eq. (2), a Poisson pseudo-equation is then solved to get the potential auxiliary function Φ^{n+1} as

$$\nabla \cdot \left(\frac{1}{\rho}\nabla \Phi^{n+1}\right) = \frac{1}{\Delta t}\nabla \cdot \widehat{\mathbf{V}}^{n+1}. \tag{12}$$

5. The pressure $P^{n+1/2}$ and the divergence-free velocity $\mathbf{V}^{n+1}$ are then obtained from the potential auxiliary function Φ^{n+1}

$$P^{n+1/2} = P^{n-1/2} + \Phi^{n+1}, \tag{13}$$

$$\mathbf{V}^{n+1} = \widehat{\mathbf{V}}^{n+1} - \frac{\Delta t}{\rho}\nabla \Phi^{n+1}. \tag{14}$$

6. Return to step 1.

3. Results

In the following sections, the numerical method described above is applied to the study of the propagation of a solitary wave over bottoms of various shapes, namely a semi-cylinder, a sloping beach and a natural beach. A schematic view of the set-up is shown in Fig. 1. The solitary wave of amplitude H in a depth h moves toward the left with a phase speed c. We define the dimensionless amplitude ϵ as $\epsilon = H/h$. An immersed object may be included in the fluid domain and is represented by the gray region in Fig. 1. The solid body may either be immersed or submerged. In the latter case (as represented in Fig. 1) the body is in contact with air and water. $\mathcal{R}$ denotes the run-up elevation.

All the computations are initialized with a solitary wave centered at the location $x = x_0$ using a second-order accurate analytical profile given by Grimshaw [46]. The initial free surface position $\eta(x, 0)$ is given by :

$$\frac{\eta(x,0)}{h} = \epsilon s^2 - \frac{3}{4}\epsilon^2 s^2 q^2 + O(\epsilon^3) \tag{15}$$

where $s = sech[\gamma(x - x_0)]$, $q = tanh[\gamma(x - x_0)]$ and $\gamma = \sqrt{(3\epsilon/4)}/h$. The phase velocity of the solitary wave is given by

$$c = c_p\left(1 + \frac{1}{2}\epsilon - \frac{3}{20}\epsilon^2\right) + O(\epsilon^3), \tag{16}$$

where $c_p = \sqrt{gh}$. The initial velocity field is also given by Grimshaw [46]. Since the analytical solution mentioned above is established using the potential flow assumption, in all the cases presented here a transitory phase is observed at early times until the boundary layer is developed at the bottom wall.

In the present configuration, the wave dynamics depends on the dimensionless amplitude $\epsilon = H/h$ and the Reynolds number here defined as [47]

$$Re = \sqrt{\frac{4}{3}}\frac{c_p h \epsilon^{3/2}}{\nu}. \tag{17}$$

The density ratio and viscosity ratio are held fixed at $\rho_w/\rho_a = 1000$ and $\mu_w/\mu_a = 55$, while ϵ and Re are varied. Physical quantities are made dimensionless using h and c as length and velocity scales, respectively, and are denoted by an asterisk. In particular, we define the dimensionless time $t^* = tc/h$ and the dimensionless coordinates, $x^* = x/h$ and $y^* = y/h$.

In the following, only two-dimensional computations are performed and no turbulence model is used. Thus, low values of Reynolds number are employed in order to guarantee the precision of the results and the stability of the computations. Numerical results presented in this paper come from four distinct computations corresponding to four different physical configurations. For each computation, the dimensions and refinement of the grid have been carefully chosen in order to guarantee an optimal resolution of the flow and to prevent side effects. The numerical properties of the grids are summarized in Table 1. The time step is updated at each iteration to guarantee the stability condition of the numerical schemes. Independently of this condition, the time step is kept below a maximum value of $\Delta t^* \leq 2.5 \times 10^{-3}$ in order to ensure the temporal precision of the computations. Details on the convergence properties of the computation in the case of a propagating solitary wave over of bottom-seated semi-circular cylinder are included in the following section.

3.1. Propagation over a bottom-seated semi-circular cylinder

A semi-circular cylinder of radius $R^* = 0.3$ is placed at the location $(x_p^* = 0, y_p^* = 0)$ in the domain as an immersed boundary. Periodic boundary conditions are imposed along the vertical walls while a no-slip (resp. free-slip) condition is imposed at the bottom (resp. top) boundary, for the velocity. A zero normal-gradient condition is imposed for the volume fraction C at both the bottom and the top boundaries.

Fig. 2 shows the computational grid around the immersed boundary. A solitary wave of amplitude $\epsilon = 0.3$ is initialized at $x^* = 14$, i.e. far enough from the cylinder so as to ensure that the transitory phase of boundary layer development takes place before the wave begins to interact with the cylinder. The Reynolds number of the solitary wave is $Re = 210$. In this section, the results are compared, when possible, to those of Klettner and Eames

Table 1
Summary of the computational grids used in the present study. Note that in irregular grid regions the grid size varies linearly.

Case	$n_x \times n_y$	Range	Grid spacing
Semi-circular cylinder	2048 × 128	$-18 < x^* < -5.2$	$\Delta x^* = 1/32$
		$-5.2 < x^* < -4.8$	$1/64 < \Delta x^* < 1/32$
		$-4.8 < x^* < 4.8$	$\Delta x^* = 1/64$
		$4.8 < x^* < 5.2$	$1/64 < \Delta x^* < 1/32$
		$5.2 < x^* < 30$	$\Delta x^* = 1/32$
		$0 < y^* < 2$	$\Delta y^* = 1/64$
Sloping beach *non-breaking case*	2696 × 80	$-3.56 < x^* < -1.56$	$1/120 < \Delta x^* < 1/10$
		$-1.56 < x^* < 10.4$	$\Delta x^* = 1/120$
		$10.4 < x^* < 76.4$	$1/10 < \Delta x^* < 1/120$
		$0 < y^* < 1$	$1/32 < \Delta y^* < 1/120$
		$1 < y^* < 2$	$1/120 < \Delta y^* < 1/32$
Sloping beach *breaking case*	2354 × 158	$-19.5 < x^* < -6.3$	$1/100 < \Delta x^* < 1/10$
		$-6.3 < x^* < 9.7$	$\Delta x^* = 1/100$
		$9.7 < x^* < 38$	$1/10 < \Delta x^* < 1/100$
		$0 < y^* < 0.7$	$1/32 < \Delta y^* < 1/100$
		$0.7 < y^* < 1.8$	$\Delta y^* = 1/100$
		$0.7 < y^* < 2.5$	$1/100 < \Delta y^* < 1/32$
Natural beach	2038 × 152	$-4 < x^* < 12$	$1/10 < \Delta x^* = 1/100$
		$12 < x^* < 36$	$1/10 < \Delta x^* < 1/100$
		$0 < y^* < 0.7$	$1/32 < \Delta y^* < 1/100$
		$0.7 < y^* < 1.8$	$\Delta y^* < 1/100$
		$0.7 < y^* < 2.5$	$1/100 < \Delta y^* < 1/32$

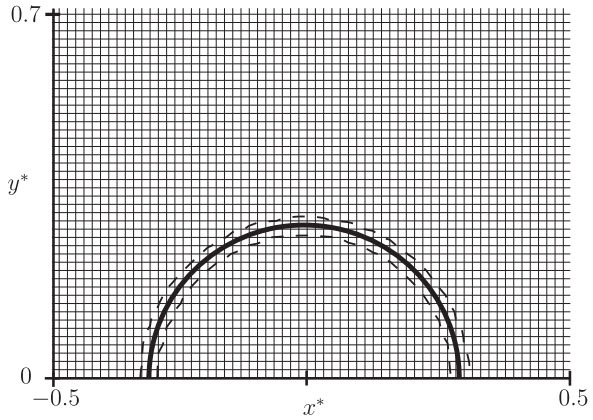

Fig. 2. Computational grid in the vicinity of the immersed boundary. The semi circular cylinder is materialized by the isolines of solid volume fraction $\alpha = 0.5$ (solid line), $\alpha = 0.05$ and $\alpha = 0.95$ (dashed lines).

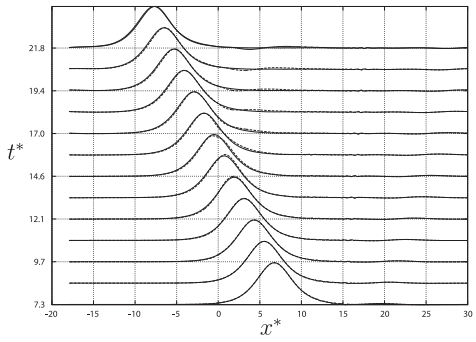

Fig. 3. Evolution of the free-surface, materialized by the iso-contour $C = 0.5$, of a solitary wave propagating over (——) a flat bottom and (------) a circular cylinder. The cylinder is at the location $x^* = 0$ and the initial location of the wave's crest is $x_0^* = 14$. Note that the vertical scale is arbitrary.

[3] who performed a direct numerical simulation of a solitary wave interacting with a semi-circular cylinder using an ALE method on a two-dimensional body-fitted grid. Their simulations were realized using 3×10^6 cells approximately. In the present work, 2.5×10^5 grid point are used.

Fig. 3 shows the evolution of the free surface ($C = 0.5$) for both the propagation over a flat bottom and over a semi-circular cylinder. The free-surface is observed to be mostly undisturbed by the presence of the immersed object. We note in passing the presence of a weakly reflected wave after $t^* \approx 14 = x_0^*/c^*$ in the case of the semi-circular cylinder.

In order to predict the wave-bottom interaction, it is important to accurately describe the flow motion in the vicinity of the solid boundary. In Fig. 4, snapshots of the vorticity field near the cylinder are presented at different times during the passage of the solitary wave. Fig. 4a confirms that the flow is essentially irrotational except near the bottom wall and the immersed cylinder. The vorticity on the top left corner of Fig. 4c and 4 d is related to the shear layer near the free surface. The regions of negative vorticity along the cylinder surface indicates the presence of two separation points : one upstream to the cylinder and one close to the top of the cylinder. The latter is responsible for the formation of a vortex at the lee side of the cylinder, which is shed from the cylinder (Fig. 4b) while other vortices are generated at the equator and are then subject to complex vortex interaction (Fig. 4c and 4 d). The present evolution of the vorticity field around the immersed cylinder is in reasonable agreement with that obtained by Klettner and Eames [3] (see their Fig. 6).

The streamlines around the semi-cylinder are presented in Fig. 5a at $t^* = 14.4$. The results are very close to those of Klettner and Eames [3] (Fig. 5b), with the presence of two recirculating regions respectively upstream and downstream to the cylinder. Some characteristics of theses regions are defined in Fig. 5c and compared for both studies in Table 2. A good agreement is observed between the two computations.

The dimensionless drag force over the cylinder is estimated as

$$F_x^* = \frac{F_x}{\frac{1}{2}\rho_l c^2 R}, \tag{18}$$

$$F_x = \int_{\mathcal{S}_p} \rho_l \mathbf{f} \cdot \mathbf{e_x} d\mathcal{S}, \tag{19}$$

with $\mathbf{f}$ being defined in (7) and $\mathcal{S}_p$ being the surface of the semi-cylinder. The temporal evolution of the force F_x^* is plotted in Fig. 6a

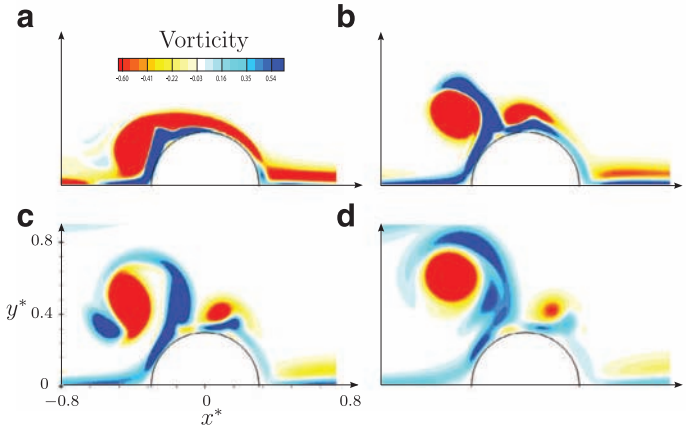

Fig. 4. (Colour online) Dimensionless vorticity field in the vicinity of a bottom-seated semi-circular cylinder during the passage of a solitary wave of amplitude $\epsilon = 0.2$ at $t^* = 17.6$ (a), 22.4 (b), 28.5 (c) and 36.3 (d). Here the vorticity is made dimensionless by c/h and the iso-contours are linearly distributed in the range $[-0.6, 0.6]$. The actual range of vorticity in each snapshot is $[-4.1, 4.9]$ (a), $[-3.7, 3.1]$ (b), $[-3.3, 1.2]$ (c) and $[-2.7, 0.8]$ (d).

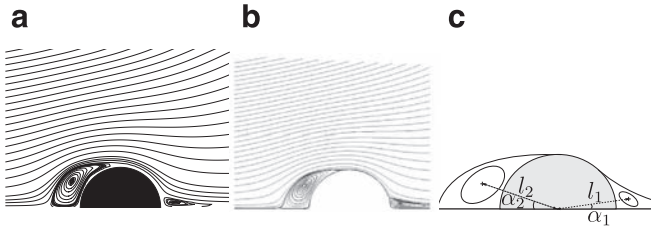

Fig. 5. Streamlines in the vicinity of the cylinder at $t^* \approx 14.4$, showing the formation of two recirculation regions stemming from the passage of the solitary wave: (a), present study. The semi-circular cylinder represented by a black disk is materialized by $\alpha = 1$; (b), results of [3] using a boundary-fitted approach; (c), schematic view of the characteristic lengths and angles used in Table 2 of the recirculation regions.

Table 2
Characteristic lengths and angles of the recirculation regions displayed in Fig. 5. The results of [3] who used a well-resolved boundary-fitted approach are taken as reference for comparison.

Study	l_1/R	l_2/R	α_1	α_2
Klettner and Eames [3]	1.26	1.25	5.9°	27.4°
Present study	1.33	1.36	5.8°	29.2°
Error (%)	5.6	8.8	2.3	6.7

and compared with that of Klettner and Eames [3]. The drag force is positive during the first instants of the computation, while the solitary wave is propagating toward the cylinder. After reaching an extremum at $t^* \approx 12$, the force then rapidly becomes positive and reaches another extremum before it goes down to zero. This behavior suggests that the drag force is mostly due to hydrostatic pressure gradient below the wave. However, in an idealized potential flow, the hydrostatic pressure gradient would result in a force F_x^* which vanishes exactly when the crest passes over the cylinder (i.e. at $t^* = x_0^*/c^*$), with equal positive and negative peaks before and after this time instance. In Fig. 6a it is observed that F_x^* does not vanish at $t^* = x_0^*/c^*$ and that the negative peak is almost twice higher than the positive one. This can be interpreted as a consequence of the presence of the viscous boundary layers. In particular, the presence of the large downstream recirculating region, as shown in Fig. 5, is expected to involve a net negative drag force.

The dimensionless spatially-averaged horizontal momentum of the solitary wave is defined as $I^* = I/cM$, where M is the mass per unit length of the wave

$$M = \int_{x_{min}}^{x_{max}} \rho_l \eta dx, \tag{20}$$

and I is the wave momentum,

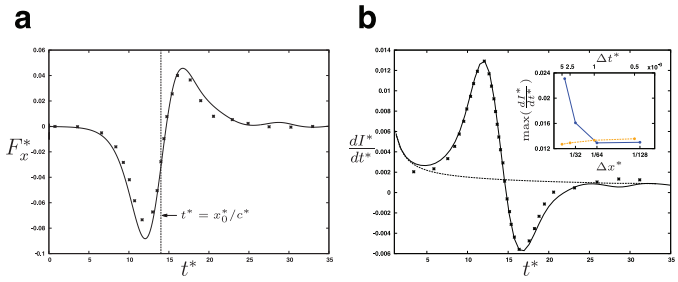

Fig. 6. Solitary wave propagating over a semi-circular cylinder: Evolution of (a) the drag force F_x^* exerted by the fluid on the cylinder, and (b) the time derivative of the spatially-averaged horizontal momentum: (——), present study; (∗), results of [3]; (------), present results for the case of a solitary wave propagating over a flat bottom. The variation of the maximum value of dI^*/dt^* as a function of the time step (------) and the grid size (——) in the region the cylinder is included in (b) to show the convergence of the computation. Here, $I^* = I/cM$.

$$I = \int_0^{\eta} \int_{x_{min}}^{x_{max}} \rho_l U dx dy. \tag{21}$$

Here x_{min} and x_{max} denote the positions of the lateral boundaries of the computation domain.

The interaction between the wave and the solid body is now observed via the variation of dI^*/dt^* (Fig. 6b). In the case of a flat bottom, one can see a transitory regime due to the adaptation of the idealized non-viscous initial condition to the bottom boundary condition. In presence of the cylinder, the time history of dI^*/dt^* is very similar to the evolution of F_x^*. A positive and a negative peak are observed, respectively corresponding to the negative and positive peak of F_x^*. After $t^* \approx 25$ the wave is not interacting anymore with the cylinder and dI^*/dt^* is the same as in the case of a flat bottom. The origin of the bump observed at $t^* \approx 30$ in Fig. 6 has not been identified so far, but may be related to the vorticity dynamics near the cylinder. During all the computation a good agreement with the results of Klettner and Eames [3] is observed despite the difference in the computation methods and in the number of cells employed.

The variation of the maximum value of dI^*/dt^* as a function of the time step and the grid size in the region of the cylinder is included in Fig. 6b to show the convergence properties of the computation. The result greatly varies with the grid size while it is less sensitive to the time step. So far, the analysis has been done on the basis of numerical results obtained with $\Delta x^* = 1/64$ and $\Delta t^* = 2.5 \times 10^{-3}$. It is seen that the computation is well converged with this set of numerical parameters.

The above observations show that the use of the present VOF-IBM approach is relevant for the numerical investigation of wave-bottom interaction problems. The method is able to accurately capture important flow features like flow separation and vortex shedding which influence the wave loading on the body, while keeping a reasonable number of grid points.

3.2. Run-up of a solitary wave on a sloping beach

In the previous section, the modeling of the free surface has not been a central issue as the wave only weakly deforms due to the presence of the cylinder. In this section, we consider the shoaling of a solitary wave on a sloping beach, which introduces additional complexity due to (i) the presence of a triple point at the coastline and (ii) the occurrence of strong free-surface deformations with possible wave breaking.

A solitary wave of amplitude ϵ and initially centered at $x_0^* = 50$ propagates toward the left before its encounters at $x_p^* = 1/tan(\beta)$ a sloping beach forming an angle $\beta = \arctan(1/19.85)$ with the horizontal axis. Free-slip boundary conditions are imposed at the upper horizontal and the vertical boundaries for the velocity, while a no-slip boundary condition is imposed at the bottom boundary. Zero normal-gradient conditions are imposed at all boundaries for the volume fraction C.

We define the wave run-up $\mathcal{R}$ as the maximum height reached by the wedge of water that climbs the beach (see e.g. Fig. 1). Synolakis [48] derived a solution based on the inviscid shallow-water theory for the run-up of a non-breaking solitary wave as a function of the amplitude and the slope *viz*

$$\frac{\mathcal{R}}{h} = 2.831(\cot\ \beta)^{\frac{1}{2}}\left(\frac{H}{h}\right)^{\frac{5}{4}}. \tag{22}$$

He also stated that the occurrence of wave breaking only depends on these parameters. His theoretical analysis allowed him to predict the critical amplitude H_c above which wave-breaking occurs, namely

$$\frac{H_c}{h} = 0.8183(\cot\ \beta)^{-\frac{10}{9}}. \tag{23}$$

We first consider a non-breaking solitary wave of amplitude $\epsilon = 0.019$. The value of the Reynolds number defined in (17) is $Re = 335$. The temporal evolution of the free-surface along the slope is presented in Fig. 7 together with the experimental data of Synolakis [40]. In order to estimate the numerical thickness of the free-surface relative to the wave amplitude, the interface is represented by three iso-lines of volume fraction. It appears that for such a small amplitude, the thickness of the free-surface and the wave amplitude are of the same order of magnitude. In practice, the free-surface is considered to be localized along the iso-line $C = 0.5$.

The present numerical solution displayed in Fig. 7 shows a good agreement with experiments. The dynamics of the shoaling is well described, except at late times during the backwash ($80 \leq t^* \leq 90$) for which there is a slight time delay between the numerical solution and the experimental data. In addition, the run-up of the wave is slightly under-predicted by the computation, since we obtain a value of $\mathcal{R}/h = 0.059$ (calculated with the iso-value $C = 0.5$ of the water volume fraction) instead of $\mathcal{R}/h = [0.076 - 0.078]$ in the experiments of Synolakis. Eq. (22), based on an inviscid theory, predicts a run-up $\mathcal{R}/h = 0.089$.

When the wave propagates over an entirely immersed body, as in the case of the bottom-seated cylinder (see Section 3.1), the air/water and water/bottom interfaces never intersect contrary to the present case where both interfaces intersect. The volume fraction as well as the sloping beach near this point are shown in Fig. 8. This figure shows that the interface is smeared in the region of the run-up. This smearing is inherent of the front-capturing

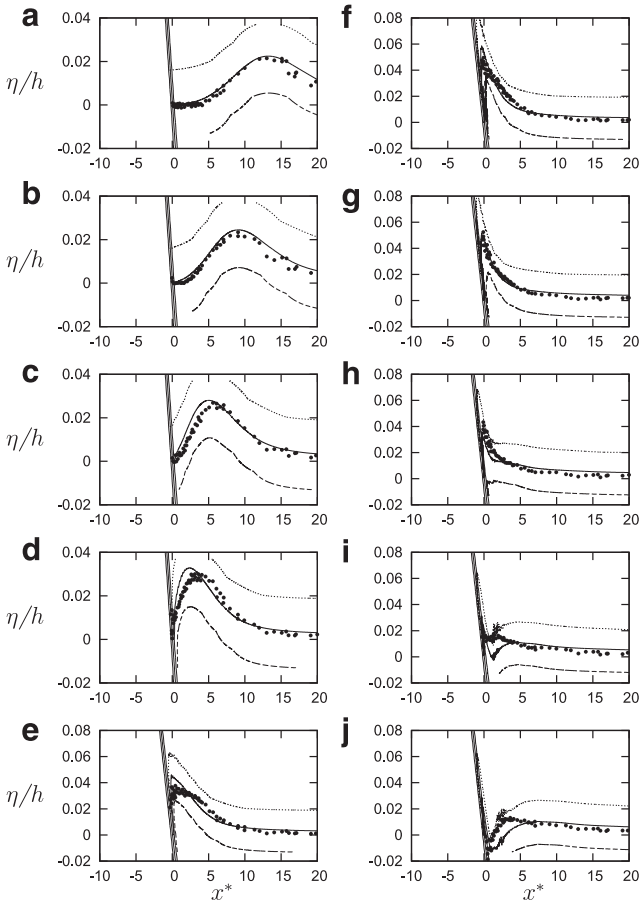

Fig. 7. Run-up of a solitary wave on a slope of angle $\beta = \arctan(1/19.85)$ with $\epsilon = 0.019$ and $Re = 335$. The free-surface for the present method is represented by iso-lines of $C = 0.1$ (▬ ▬ ▬), 0.5 (▬▬▬) and 0.9 (.....); (•), experiments of Synolakis [48]. The immersed boundary is represented by iso-lines $\alpha = 0.1$, 0.5 and 0.9. Profiles are shown at (a) $t^* = 38.01$, (b) 43.60, (c) 50.30 , (d) 55.89, (e) 61.48, (f) 68.19, (g) 72.66, (h) 78.25, (i) 82.72 and (j) 88.31. Note that the frames have been stretched in the vertical direction for sake of clarity.

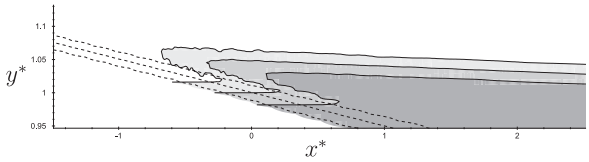

Fig. 8. Run-up of a non-breaking solitary wave on a sloping beach. Visualization of the fluid and solid volume fraction fields in the swash zone at $t^* = 62.60$. Both quantities are respectively represented with iso-contours of $C = 0.1$, 0.5, 0.9 (solid lines) and $\alpha = 0.1$, 0.5 and 0.9 (dashed lines).

methods with no interface reconstruction in regions of high shear-stress [42]. We verified that the smearing of the air-water interface was not due to the presence of the immersed-boundary, since the same distribution of volume fraction was found when the beach is treated by a boundary fitted grid with a no-slip boundary condition (not shown here).

Increasing the wave amplitude while keeping the same angle for the sloping beach leads to the breaking of the solitary wave. The occurrence of breaking is intrinsically linked to the nonlinearity of the wave propagation. During shoaling, the information propagates faster at the top of the wave, resulting in high velocity gradients in the vicinity of the crest and increasing turbulence, as observed in the Particle Image Velocimetry measurements of Kang et al. [49]. This process may then be followed by the formation of a plunging jet which involve strong mixing and

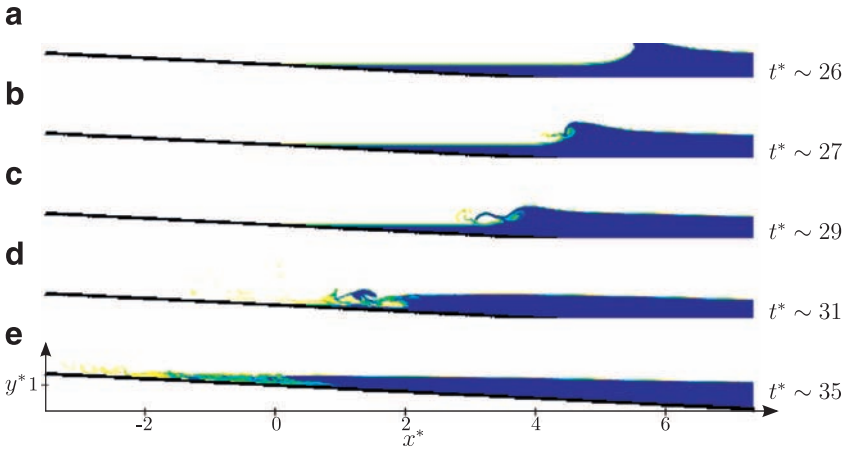

Fig. 9. Run-up of a breaking solitary wave with $\epsilon = 0.3$ and $Re = 210$, materialized by the volume fraction of water.

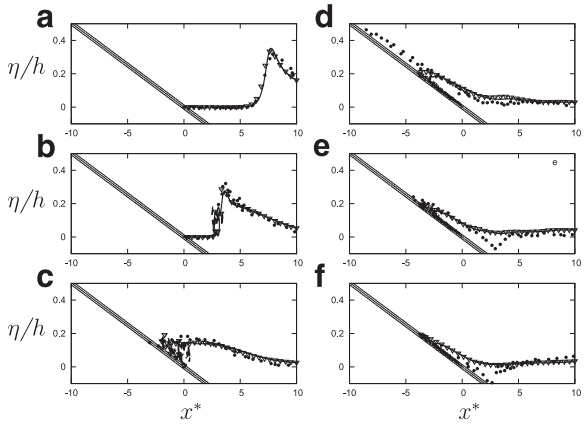

Fig. 10. Run-up of a breaking solitary wave on a slope of angle $\beta = \arctan(1/19.85)$ with $\epsilon = 0.3$ and $Re = 210$. The immersed boundary is represented by iso-lines of $\alpha = 0.1$, 0.5 and 0.9 while the free-surface obtained from the simulations is materialized by the iso-contour $C = 0.5$: (——) present method with the beach treated as an immersed boundary; (•) experiments of [40]; (∇) present method with the beach treated as a body-fitted boundary with a no-slip condition for the velocity. Profiles are shown at times (a) $t^* = 23.91$, (b) 28.97 , (c) 34.64, (d) 57.25, (e) 68.58 and (f) 79.91. Note that the frames have been stretched in the vertical direction for clarity.

the generation of turbulence. Recall that here, we intend to solve all the spatial and temporal scales of the flow by means of direct numerical simulation, i.e. without using any turbulence model. The limited computational resources force us to choose moderate values of the Reynolds number.

We performed a simulation of the propagation of a solitary wave of amplitude $\epsilon = 0.3$ and Reynolds number $Re = 210$ running up a sloping beach with an angle $\beta = \arctan(1/19.85)$. As the amplitude ϵ of the wave is well above the critical amplitude given by Eq. (23) $H_c/h = 0.03$, the wave is expected to break during the run-up. In Fig. 9, we plot the temporal evolution of the wave shape. Despite the moderate value of the Reynolds number, one can observe a typical plunging break down of the wave. In Fig. 9a, a plunging jet impacts the free-surface, causing the formation of a secondary jet (splash-up, Fig. 9b). This results in mixing between air and water as observed in Fig. 9c and 9 d. This is in agreement with experimental observations of Bonmarin [50].

The free-surface position during the run-up ($C = 0.5$) is compared with the experimental results of Synolakis [40] in Fig. 10. Note that in the experiment, $Re \approx 5 \times 10^4$. A very good agreement is observed for $t^* \leq 35$, i.e. before the collapsing of the bore and the ejection of the jet [51]. At $t^* = 57.25$, the run-up is underpredicted by the computation in comparison with the experiments. In addition, the bore located at $x^* = 3$ for $t^* = 70 - 80$ in the experiments due to the backwash flow is not observed in the simulation. Note however, that this region connecting the backward flowing thin layer of water and the deeper water is likely to be subject to strong mixing and air entrainment, thus increasing the experimental uncertainties of the free-surface measurements.

In order to assess the influence of the immersed boundary on the solution, we performed another computation for which the beach is treated as a boundary-fitted grid with a no-slip (resp. zero-normal gradient) condition imposed for the velocity (resp. volume fraction). The profiles of the free-surface running up the body-fitted beach is shown in Fig. 10 (triangle symbols). It is found that the free-surface profile is nearly identical to that obtained with the simulation for which the beach is modeled via an immersed boundary. Therefore, one may conclude that the discrepancy between the simulation and the experiment is not due to the immersed-boundary modeling.

The discrepancy observed between the numerical simulation and the experience is likely due to the difference of Reynolds numbers. Recall that $Re = 210$ ($Re \approx 5 \times 10^4$) in the simulations (experiments). The somewhat low value of the Reynolds number employed in the computation may lead to an increased energy dissipation in the regions of high velocity gradients especially at the air-water interface and more importantly along the wall of the sloping beach. During the run-up of the water front, the viscous dissipation becomes significant in the thin layer of water which is subject to strong shear at both the air-water interface and at the wall. In the case of thin liquid fronts propagating along a horizontal wall, Bonometti et al. [52] showed that the wall friction could lead to a decrease of the front velocity of up to 50% especially when the density ratio of the current to ambient is large, as in the present case. This is in line with the fact that the discrepancy between the simulations and the experiment in Fig. 10 is probably due to viscous friction (along the sloping beach) which is artificially increased by the somewhat low value of the chosen Reynolds number.

An indirect confirmation of this point is given in Fig. 11 where the beach is still treated by a body-fitted mesh but with a free-slip boundary condition (i.e. no viscous stress at the boundary). Here, we observed a close agreement with experiments. The dynamics of both the run-up and rundown is well described, including the formation of a bore during the backwash, even though its position is slightly shifted toward the shore (Fig. 11e). This confirms that the small run-up of the computed wave front in Fig. 10 is related to the artificially large wall friction along the beach and not to the fact that the beach is modeled by an immersed boundary.

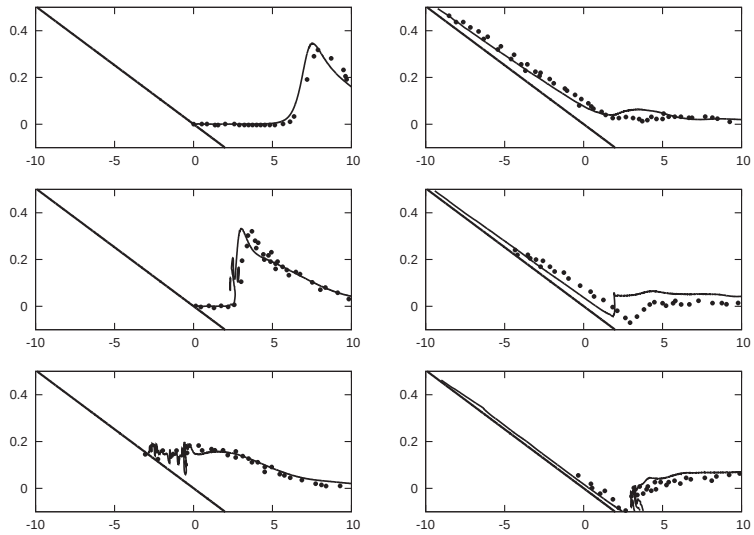

Fig. 11. Same as Fig. 10: (•) experiments of [40]; (——) present method with the beach treated as a body-fitted boundary with a free-slip condition for the velocity.

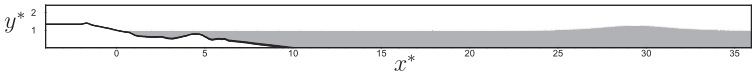

Fig. 12. Visualization of the initial state of the simulation of the run-up of a solitary wave on a natural beach. The two fluid phases are represented in gray (water) and white (air), respectively and the immersed boundary (i.e. the beach) is represented by the solid black line. Here, the wave amplitude is $\epsilon = H/h = 0.27$.

In summary, the above observations allow us to conclude that (i) the VOF method is efficient in describing complex interface deformations including plunging wave breaking, the dynamics of a free-surface of small amplitude being well captured even with a moderate spatial resolution of the free surface; (ii) the IBM is able to reproduce wave-body interactions including non-breaking and breaking waves running up a sloping beach; (iii) a low value of the Reynolds number leads to large viscous wall friction inside the climbing layer of fluid along the slope. Setting a free-slip boundary condition along the beach permits to get good agreement between moderate-*Re* simulation and water wave experiments.

3.3. Run-up of a solitary wave on a natural beach

So far the present numerical method was applied to academic cases usually considered as paradigms of more complex natural configurations. The advantage of the immersed boundary method as compared to approaches using a body-fitted grid is that it can be applied to arbitrary bottom geometries. In order to illustrate the potential of such a method, we now focus on the run-up of a breaking solitary wave on a natural beach.

Caplain [53] performed a series of experiments in order to study sediment transport and sea bed morphology induced by a harmonic wave forcing. Different types of beach profile were obtained depending on the energy of the incoming waves. These profiles were mostly two-dimensional, that is invariant along the horizontal direction perpendicular to the incoming waves. For our numerical simulation, we chose one profile as an example of a naturally shaped beach (see Fig. 4.11 in [53]). A visualization of the beach modeled via an immersed boundary in the computational domain is presented in Fig. 12. Note that we extended the left part of the beach by a plateau ($x^* \leq 2$) in order to permit overflow.

The solitary wave is initialized with an amplitude $\epsilon = 0.27$ corresponding to a Reynolds number $Re = 360$. Snapshots of volume fraction at different time during the run-up are shown in Fig. 13. At $t^* = 26.1$, the wave has passed the bar and lost its initial shape, mostly due to the blocking effect caused by the topographical bump. At $28.6 \leq t^* \leq 29.5$, a bore is formed which collapses at $t^* \approx 30.2$. In the present case, the run-up of the wave is large and induces an overflow visible at $t^* = 33.9$. Note that this overflow is likely to be under predicted due to the low value of the Reynolds number used here, as discussed in the previous section.

The profile of the free surface exhibits other complex interactions between the wave and the topography. An interesting feature is the presence of a deformation of the free surface on the left side of the bar ($x^* \approx 3.5$) which appears at $t^* = 28.6$ and persists for a long time after the passage of the crest (until $t^* = 40$). The depression is located above a strong decrease of the bottom floor at the left of the bump. This perturbation remains stationary until the primary wave reaches its maximum run-up distance, and then propagates back offshore ($33.9 \leq t^* \leq 41.3$). The Froude number associated with the solitary wave can be estimated by $F = \mathcal{U}/\sqrt{gh}$, $\mathcal{U}$ being the characteristic velocity of the solitary wave namely $\mathcal{U} = \epsilon\sqrt{gh}$, which leads to $F = \epsilon = 0.27$. In addition, the blockage factor defined as the height ratio between the bar and the free surface is approximately 80%, here. Similar features were observed in subcritical free surface flows over an obstruction with a high blockage factor, as in [54] and [55] for example.

A typical feature of the flow induced by the run-up is shown in Fig. 14. The flow structure in the vicinity of the bar, which is oriented from rigth to left, is characterized by two recirculation regions. On the lee side of the bar, we observe the formation of a strong vortex which persists until it is swept down when the wave begins to rundown (not shown). The flow pattern described here has a great importance in terms of bed load transport, as one would expect such structures to result in a sharpening of the bar. In order to quantitatively illustrate this feature, we show in Fig. 14 the bottom shear stress $\tau_b = \mu\partial u_t/\partial n$, interpolated on the isoline $\alpha = 0.5$ in the vicinity of the bar. Here u_t and n respectively denote the tangential velocity and the direction normal to the bottom. We observe that two extrema of opposite sign ($\tau_b \approx \pm 1$) are present on both sides of the top of the bar. A rough estimation of the Shields parameter $\Theta = \tau_b/(\rho_s - \rho)gD$ based on the characteristic sediments density ρ_s and diameter D of the particles used in

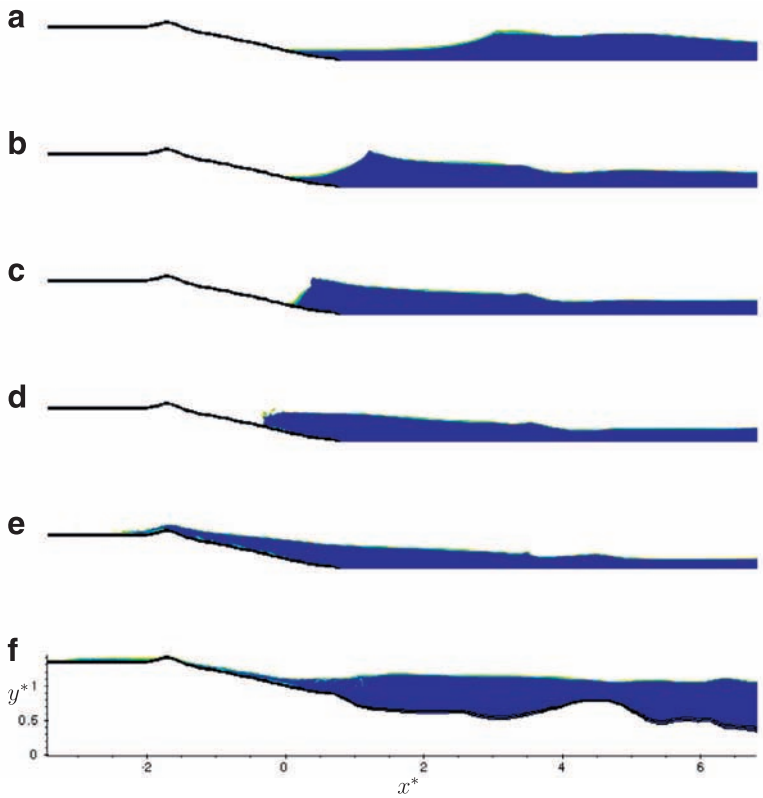

Fig. 13. Run-up of a breaking solitary wave on a natural beach. Snapshots of volume fraction at $t^* = 26.1$ (a),28.6 (b), 29.5 (c), 30.2 (d), 33.9 (e) and 41.3 (f). Note that the aspect ratio of the snapshots is here equal to 1.

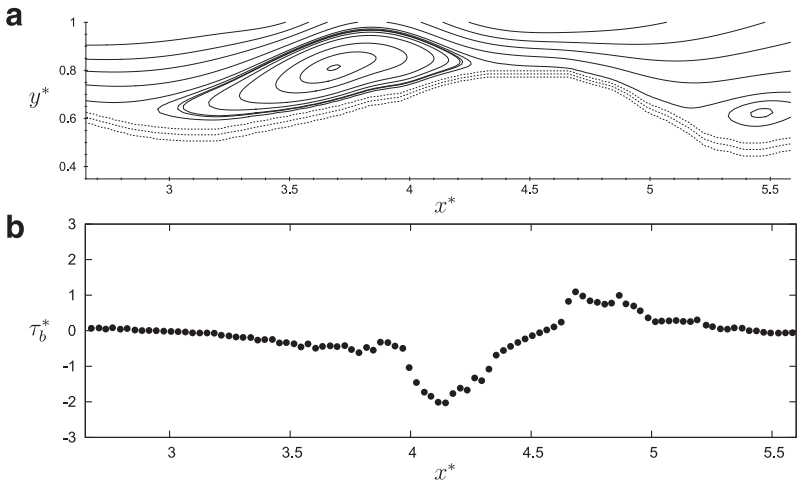

Fig. 14. Run-up of a breaking solitary wave on a natural beach. Streamlines (a) and bottom shear stress (b) in the vicinity of the bar at $t^* = 31.6$.

the experiments of [53] gives $\Theta \approx 0.2$ for $\tau_b = 1$. Considering a critical value $\Theta_c = 0.1$ above which a particle suspension may be expected, the present flow would result in a sediment transport from both sides of the bar toward the top. A similar approach has been used by [56] in order to simulate the morphodynamic in an open-channel bend.

4. Summary and conclusions

The aim of this work was to demonstrate the capability of a coupled VOF-IBM numerical method to accurately reproduce wave shoaling on simple and complex shaped bottoms. The propagation of a solitary wave over a semi-circular cylinder has been simulated showing that the IBM was able to reproduce some key features of fluid-body interaction such as flow separation and vortex shedding. Quantitative comparison with the results of [3] shows that the flow dynamics is well described even if the spatial resolution is one order of magnitude lower than that used by these authors.

The present approach was then applied to the run-up of a solitary wave on a sloping beach where strong deformations of the free surface occur, including plunging wave breaking and generation of secondary jets. The low value of the Reynolds number employed in the simulations has been identified to be the cause of an under prediction of the maximum wave run-up due to an artificially increased wall friction along the slope of the beach. Comparisons with boundary-fitted simulations with no-slip and free-slip condition along the beach slope have shown that (i) the immersed boundary is able to reproduce the no-slip condition along the

immersed boundary and (ii) using a free-slip boundary enables us to obtain a good agreement with experimental results despite the somewhat low value of the Reynolds number.

Finally, we presented a simulation of the run-up of a breaking solitary wave on a natural beach including the presence of a bar in the breaker zone. We observed that complex interaction take place in this region. The free-surface dynamics is characterized by the presence of a stationary perturbation similar to those observed in channel flows over an obstacle, and the formation of two recirculating regions around the bar's crest associated with the formation of strong vortices.

The capability of the IBM to deal with arbitrary shaped boundaries widely increases the diversity of problems which can be studied numerically. Then, as both the VOF method and the IBM can be straightforwardly applied to three-dimensional configurations, numerical studies of wave shoaling over variable topography along both directions can be performed.

References

[1] Liu Y, Dommermuth D, Yue D. A high-order spectral method for nonlinear wave body interactions. J Fluid Mech 1992;245:115–36.
[2] Lin M, Huang L. Study of water waves with submerged obstacles using a vortex method with Helmholtz decomposition. Int J Numer Meth Fluids 2009;60:119–48.
[3] Klettner C, Eames I. Momentum and energy of a solitary wave interacting with a submerged semi-circular cylinder. J Fluid Mech 2012;708:576–95.
[4] Longuet-Higgins M, Cokelet E. The deformation of steep surface waves on water. I. a numerical method of computation. Proceedings of the Royal Society London A 1976;350:1–26.
[5] Dold J, Peregrine D. An efficient boundary integral method for steep unsteady water waves. Numer Meth Fluid Dynam II 1986:671–9.
[6] Chian C, Ertekin R. Diffraction of solitary waves by submerged horizontal cylinders. Wave Motion 1992;15:121–42.
[7] Grilli S, Subramanyan R, Svendsen I, Veeramony J. Shoaling of solitary waves on plane beaches. J Waterw Port C Ocean Eng 1994;120:609–28.
[8] Dommermuth D, Yue D. A high-order spectral method for the study of nonlinear gravity waves. J Fluid Mech 1987;184:267–88.
[9] Craig W, Sulem C. Numerical simulation of gravity waves. J Comput Phys 1993;108:73–83.
[10] Bateman W, Swan C, Taylor P. On the efficient numerical simulation of directionally spread surface water waves. J Comput Phys 2001;174:277–305.
[11] Nicholls D. Traveling water waves: spectral continuation methods with parallel implementation. J Comput Phys 1998;143:224–40.
[12] Liu Y, Yue D. On generalized Bragg scattering of surface waves by bottom ripples. J Fluid Mech 1998;297:297–356.
[13] Smith R. An operator expansion formulation for nonlinear surface water waves over variable depth. J Fluid Mech 1998;363:333–47.
[14] Iafrati A, Campana E. A domain decomposition approach to compute wave breaking (wave-breaking flows). Int J Numer Meth Fluids 2003;41:419–45.
[15] Grilli S, Harris J, Greene N. Modeling of wave-induced sediment transport around obstacles. In: Proceedings of the 31st International Conference on Coastal Engineering; 2008. p. 1638–50.
[16] Zhang Y, Peszynska M, Yim S. Coupling of viscous and potential flow models with free surface for near and far field wave propagation. Int J Numer Anal Model 2013a;4(3):256–82.
[17] Lin M, Huang L. Vortex shedding from a submerged rectangular obstacle attacked by a solitary wave. J Fluid Mech 2010;651:503–18.
[18] Pedersen G, Gjevik B. Run-up of solitary waves. J Fluid Mech 1983;135:283–99.
[19] Madsen P, Fuhrman D, Wang B. A Boussinesq-type method for fully nonlinear waves interacting with a rapidly varying bathymetry. Coastal Eng 2006;53:487–504.
[20] Hibbert S, Peregrine D. Surf and run-up on a beach: a uniform bore. J Fluid Mech 1979;95:323–45.
[21] Zhang J. Run-up of ocean waves on beaches. California Institute of Technology, Pasadena, CA; 1996. Ph.D. thesis.
[22] Dodd N. Numerical model of wave run-up, overtopping, and regeneration. J Waterw Port C Ocean Eng 1998;124:73–81.
[23] Titov V, Synolakis C. Modeling of breaking and non-breaking long-wave evolution and run-up using VTCS-2. J Waterw Port C Ocean Eng 1995;121:308–461.
[24] Li Y, Raichlen F. Non-breaking and breaking solitary wave run-up. J Fluid Mech 2002;456:295–318.
[25] Tang C, Chang J. Flow separation during solitary wave passing over submerged obstacle. J Hydraul Eng 1998;124:742–9.
[26] Zhang D, Chwang A. On solitary waves forced by underwater moving objects. J Fluid Mech 1999;389:119–35.
[27] Lo D, Young D. Arbitrary Lagrangian-Eulerian finite element analysis of free surface flow using a velocity-vorticity formulation. J Comput Phys 2004;195:175–201.
[28] Zhao Q, Tanimoto K. Numerical simulation of breaking waves by large eddy simulation and VOF method. In: Proceedings of the 26th International Conference on Coastal Engineering, 1; 1998. p. 892–905.
[29] Hieu P, Tanimoto K, Ca V. Numerical simulation of breaking waves using a two-phase flow model. Appl Math Model 2004;11:983–1005.
[30] Zhao Q, Armfield S, Tanimoto K. Numerical simulation of breaking waves by multi-scale turbulence model. Coastal Eng 2004;51:53–80.
[31] Lubin P, Glockner S, Kimmoun O, Branger H. Numerical study of the hydrodynamics of regular waves breaking over a sloping beach. Eur J Mech B-Fluids 2011;30:552–64.
[32] Chang K, Hsu T, Liu P. Vortex generation and evolution in water waves propagating over a submerged rectangular obstacle: Part I. Solitary waves. Coastal Eng 2001;44:13–36.
[33] Lin P. A numerical study of solitary wave interaction with rectangular obstacles. Coastal Eng 2004;51:35–51.
[34] Sue Y, Chen M, Hwang R. Interaction of nonlinear progressive viscous waves with a submerged obstacle. Ocean Eng 2005;32:893–923.
[35] Peng W, Lee K-H, Mizutani N. Application of direct-forcing IB-VOF method to the simulation of wave deformation by submerged structures. J Coastal Res 2012;28(3):658–70.
[36] Shen L, Chan E-S. Numerical simulation of fluid–structure interaction using a combined volume of fluid and immersed boundary method. Ocean Eng 2008;35(8):939–52.
[37] Lee K-H, Mizutani N. A numerical wave tank using direct-forcing immersed boundary method and its application to wave force on a horizontal cylinder. Coastal Eng J 2009;51(01):27–48.
[38] Zhang C, Zhang W, Lin N, Tang Y, Zhao C, Gu J, et al. A two-phase flow model coupling with volume of fluid and immersed boundary methods for free surface and moving structure problems. Ocean Eng 2013b;74:107–24.
[39] Zhao X., Gao Y., Cao F., Wang X.. Numerical modeling of wave interactions with coastal structures by a constrained interpolation profile/immersed boundary method. Int J Numer Meth Fluids, in press.
[40] Synolakis C. The run-up of long waves. California Institute of Technology, Pasadena, CA; 1986. Ph.D. thesis.
[41] Bigot B, Bonometti T, Lacaze L, Thual O. A simple immersed-boundary method for solid-fluid interaction in constant- and stratified-density flows. Comput Fluids 2014;97:126–42.
[42] Bonometti T, Magnaudet J. An interface-capturing method for incompressible two-phase flows. Validation and application to bubble dynamics. Int J Multiphas Flow 2007;33:109–33.
[43] Harlow F, Welch J. Numerical calculation of time-dependent viscous incompressible flow of fluid with free surface. Phys Fluids 1965;8:2182–9.
[44] Calmet I, Magnaudet J. Large-eddy simulation of high-Schmidt number mass transfer in a turbulent channel flow. Phys Fluids (1994-present) 1997;9(2):438–55.
[45] Zalesak S. Fully multidimensional flux-corrected transport algorithms for fluids. J Comput Phys 1979;31:335–62.
[46] Grimshaw R. The solitary wave in water of variable depth. J Fluid Mech 1971;46:611–22.
[47] Sumer B, Jensen P, Sorensen L, Fredsoe J, Liu P. Turbulent solitary wave boundary layer. In: Proceedings of the 18th International Offshore and Polar Engineering Conference; 2008. p. 775–81.
[48] Synolakis C. The run-up of solitary waves. J Fluid Mech 1987;185:523–45.
[49] Kang D, Ghosh S, Reins G, Koo B, Wang Z, Stern F. Impulsive plunging wave breaking downstream of a bump in a shallow water flum - Part I: Experimental observations. J Fluid Struct 2012;32:104–20.
[50] Bonmarin P. Geometric properties of deep-water breaking waves. J Fluid Mech 1989;209:405–33.
[51] Mory M, Abadie S, Mauriet S, Lubin P. Run-up flow of a collapsing bore over a beach. Eur J Mech B-Fluids 2011;30(6):565–76.
[52] Bonometti T, Balachandar S, Magnaudet J. Wall effects in non-boussinesq density currents. J Fluid Mech 2008;616:445–75.
[53] Caplain B. Étude expérimentale de l'érosion d'un massif de sable cohésif par une houle monochromatique. Institut National Polytechnique de Toulouse, France; 2011. Ph.D. thesis.
[54] Forbes L. Critical free-surface flow over a semi-circular obstruction. J Eng Math 1988;22:3–13.
[55] Vigie F. Etude expérimentale d'un écoulement à surface libre au-dessus d'un obstacle. Institut National Polytechnique de Toulouse, France; 2005. Ph.D. thesis.
[56] Khosronejad A, Kang S, Borazjani I, Sotiropoulos F. Curvilinear immersed boundary method for simulating coupled flow and bed morphodynamic interactions due to sediment transport phenomena. Adv Water Resour 2011;34(7):829–43.